View Article Online
DOI: 10.1039/D0TA07347D

ARTICLE

Composite cathode material encapsulated by amorphous garnet-type solid electrolyte and self-assembled $La_2(Ni_{0.5}Li_{0.5})O_4$ nanoparticles for all-solid-state batteries

Received 00th January 20xx,
Accepted 00th January 20xx

DOI: 10.1039/x0xx00000x

Kookjin Heo,[a,b] Jonggwan Lee,[a,c] Jehong Im,[a] Min-Young Kim,[a] Ho-Sung Kim,[d] Docheon Ahn,[e] Jaekook Kim[b] and Jinsub Lim*[,a]

In this article, we report the effect of surface modification of NCM80 [$Li(Ni_{0.8}Co_{0.1}Mn_{0.1})O_2$] cathode material on the performance of all-solid-state batteries (ASSBs) with oxide-based organic/inorganic hybrid solid electrolytes. Ni-rich cathode material $Li(Ni_xCo_{(1-x)//2}Mn_{(1-x)/2})O_2$ (x>0.6) (NCM) with high specific capacity and a layered structure is a suitable cathode material for next-generation energy storage systems, particularly electric vehicles and portable device, for the ASSBs. However, for the ASSBs, resistance at the interface between cathode and solid electrolyte is larger than that of the liquid electrolyte because of point contact. To solve this problem, we fabricated a composite cathode material encapsulated by amorphous garnet-type solid electrolyte and $La_2(Ni_{0.5}Li_{0.5})O_4$ nanoparticles. Therefore, the structure, cycling stability, and rate performance of the composite-NCM80 cathode material in ASSBs with oxide-based organic/inorganic hybrid electrolytes were investigated using powder X-ray diffraction analysis, field-emission scanning electron microscopy, electrochemical impedance spectroscopy, and galvanostatic measurements.

Keywords: Li-ion Batteries, surface modification, all-solid-state battery

Introduction

Recently, lithium ion secondary batteries (LIBs) have been widely used as a power source for portable electric device, such as mobile phone, laptop, and electric vehicles, because of their high energy and power density. However, popularized commercial LiBs are exposed to risks, such as leakage, fire, and explosion, which are based on flammable organic liquid electrolytes [1-3]. These safety issues can cause problems when using LIBs to develop large-scale batteries for applications such as energy storage system and electric vehicles. Hence, all-solid-state batteries (ASSBs) are being considered as a next-generation secondary batteries because they can replace flammable organic liquid electrolytes with non-flammable organic solid electrolytes, which can act as an electrical insulator and ionic conductor simultaneously and improve the safety and energy density of the batteries. Hence, the ASSBs using solid electrolyte (SE) have recently attracted great interest because of their favorable features, including lack of electrolyte leakage and wide potential window. [4-6]

There are two major types of solid electrolyte: inorganics (ceramics and glasses) and polymer; inorganic solid electrolytes are further divided into sulfides and oxides. The manufacturing process of sulfide-based solid electrolyte, such as $Li_{10}GeP_2S_{12}$ (LGPS) and Li_6PS_5Cl (LPSCl), is complex because they produce toxic H_2S gases due to the reaction with moisture present in the atmosphere [7-9]. Oxide-based solid electrolytes exhibits good chemical stability against air and compatibility with high voltage cathode material compared to sulfide-based solid electrolyte. The oxide-based solid electrolyte is divided into NASICON-type ($Li_{1+x}Al_xTi_{2-x}(PO_4)_3$ (LATP)), Perovskite-type ($Li_{3-x}La_{2/3-x}TiO_3$ (LLTO)), and Garnet-type ($Li_7La_3Zr_2O_{12}$ (LLZO)) according to their crystal structure [10-14]. However, here are major issue for oxide-based solid electrolyte. First one is the generally low ionic conductivity, which is lower than that of sulfide electrolytes at room temperature. Despite of the phenomenally low intrinsic bulk conductivity, recent investigations point to the high interface polarization that restrains battery dynamics. Secondly, due to the rigid of ceramic nature, it cause poor point contact at electrode and electrolyte interface. However, oxide-based solid electrolyte have a key advantage of intrinsic wide electrochemical potential window. For a garnet type LLZO, it has wide potential window as 0 – 6 V. For the more, it is attractive candidate solid electrolyte due to its high RT ionic conductivity (~ 1mS cm-1), and chemical stability against Li metal.[14-16].

These inorganic ceramic electrolytes are generally rigid and brittle with low flexibility, which cause poor contact and high

[a] Korea Institute of Industrial Technology (KITECH), 6, Cheomdan-gwagiro 208-gil, Buk-gu, Gwangju 61012, Republic of Korea
[b] Department of Materials Science and Engineering, Chonnam National University, 300 Yongbongdong, Bukgu, Gwangju 61186, Republic of Korea
[c] Department of Materials Science and Engineering, Chosun University, 309 Pilmun-daero, Dong-gu, Gwangju 61452, Republic of Korea
[d] Korea Institute of Industrial Technology (KITECH), Jeju-si Special Self-Governing Province, 63243, Republic of Korea
[e] Beamline Department, Pohang Accelerator Laboratory (PAL), Pohang, 37673, Republic of Korea
*Corresponding author: Tel.: +82-62-600-6430; fax: +82-62-600-6179.
e-mail: jinsub@kitech.re.kr (J. S. Lim)

resistance at the interface between SE and positive electrode. Solid polymer electrolytes (SPEs) exhibit high flexibility and excellent contact at the positive electrode and electrolyte interface. Polyethylene oxide (PEO), polyethylene glycol (PEG), polypropylene chloride (PPC), polyvinylidene fluoride (PVDF), polyvinylpyrrolidone (PVP), polyacrylonitrile (PAN), and sulfonated poly(ether ether ketone) (SPEEK) [17-23] have been widely used as a polymer electrolytes. Among them, PEO-based SPE is widely studied as a most promising candidate for a ASSBs because of its benefits; easy to fabrication, low cost and excellent compatibility with lithium salt. And, Li^+ ions can move within the free volume of the polymer host assisted by the movement of the polymer chains when the temperature exceeds the T_g (glass transition temperature). Li^+ ions were coordinated by ether oxygen and transport with the breaking/forming of Li-O bonds. [17]

To address the limitation of pure polymer and inorganic ceramic electrolyte, inorganic particle and polymer Li salt matrix are widely studied to integrate the merits of the components. Inorganic nanoparticles play an important role as ionic conducting fillers in PEO-based composite electrolytes, enhancing their electrochemical properties. The PEO-Li salt matrix reduces the interfacial resistance owing to its fast Li-ion conduction pathways, resulting in improved ASSB electrochemical performance [17]. Sun. et al reported an inorganic-polymer composite solid electrolyte, synthesized by adding LATP nanoparticles to PEO-$LiClO_4$ matrix that shows high lithium ionic conductivity of 1.6 x 10^{-3} s cm^{-1} at 80 °C [17]. D. H. Kim et al. reported that the composited nano-sized LLZO in an inorganic-organic hybrid composite membrane exhibits high ionic conductivity (1.93 × 10^{-3} S cm^{-1} at 70 °C) due to the synergy of the LLZO inorganic filler in the composite membrane [19]. Therefore, the PEO-based inorganic–polymer composite electrolyte is a promising solid electrolyte for next-generation ASSBs with high energy density and high power density.

In the positive electrode for ASSBs, efficient contact between active material and solid electrolyte is very important. ASSB provides three main components; positive electrode, negative electrode and solid electrolyte. During charging/discharging, lithium ion moves to the positive electrode through the solid electrolyte extracted from the negative electrode. Since the movement of lithium ions proceeds at the interface between the solid electrolyte and the positive electrode active material, stable and intimate interface is required for the reaction step to proceed smoothly. Interfacial instability can result from chemical or electrochemical problems, the most fundamental origin is abrupt electrochemical potential changes at the electrode-electrolyte interface [20, 21]. To overcome the interface stability between positive electrode and solid electrolyte, there are method to reducing the interfacial resistance by putting into the ionic conductivity buffer layer [22-24]. H. Chen et al reported that improving the interface stability of ASSBs using an electrolyte buffer layer on the rough surface of the cathode. The buffer layer act the decrease the interfacial between the cathode and the solid electrolyte [23]. Another approach to reduce the interfacial resistance between positive electrode and solid electrolyte is coating the cathode material with an ionic conductivity materials for the ASSBs [25-34]. F. Han et al reported that an all-ceramic cathode/electrolyte with an extremely low interfacial resistance can be realized by thermally soldering $LiCoO_2$ (LCO) and LLZO together with the $Li_{2.3-x}C_{0.7+x}B_{0.3-x}O_3$ solid electrolyte interphase through the reaction between the $Li_{2.3}C_{0.7}B_{0.3}O_3$ solder and Li_2CO_3 layers that can be conformally coated on the LLZO and LCO. Further, an all-solid-state Li/LLZO/LCO battery exhibits high cycling stability and high rate performance [32]. Kim et al reported that the preparation of Li_2CO_3- and Li_2CO_3/$LiNbO_3$-coated NCM622 for application in pelletized SSB cells using β-Li_3PS_4 as the SE. The surface carbonate contaminants helps improve the cell cyclability, and the combination of carbonate and niobate species in a kind of hybrid or solid-solution coating is particularly beneficial for achieving stable performance of Ni-rich NCM composite cathodes [33].

Thus, we describe a Ni-rich cathode material designed by surface modification of ionic conductor material in an ASSB system to improve the lithium ionic conductivity between the cathode material and SE. The LLZO material is suitable for the surface modification of cathode material owing to its high ionic conductivity at room temperature. Therefore, it has been employed for surface coating on various cathode material for Libs. We previously reported that an ionic conductor-NCM80 composite was synthesized by simultaneous co-precipitation method and garnet type $Li_{6.75}La_3Zr_2Al_{0.25}O_{12}$ (LLZAO) material on the cathode material surface. The composite has a high lithium ion conductivity and aids in the lithium ion diffusion from electrode to electrolyte. The impedance spectroscopy measurement showed that it demonstrated a high Rs value than that of a NCM80 sample after the 1st cycle by acting as a small resistor of composite material. However, the resistance decreased as the cycle progressed, leading to improved rate capability and reduced Rs value [34].

Therefore, in this study, the structure and electrochemical performance of a composite-NCM80 material encapsulated by amorphous garnet-type SE and self-assembled $La_2(Ni_{0.5}Li_{0.5})O_4$ nanoparticles was investigated to be used in the ASSBs with oxide-based organic/inorganic composite SE to address the interface issue in ASSBs. Composite-NCM80 material was synthesized by simultaneous co-precipitation method. A schematic diagram of the ASSBs using composite-NCM80 material is illustrated in Fig. 1. We are manufactured the positive electrode and solid electrolyte sheet using the organic/inorganic solid electrolyte based on PEO binder. In the case of LIBs, the cell is composed of a positive electrode, separator, negative electrode and liquid electrolyte. However, in the case of all-solid-state battery, solid electrolyte is used instead of separator. This solid electrolyte which an organic/inorganic solid electrolyte sheet composed of LLZO solid electrolyte, PEO binder and $LiClO_4$ lithium salt was prepared. In addition, LLZO solid electrolyte included in the positive electrode, since a liquid electrolyte is not used in an all-solid-state battery, LLZO is added to facilitate the movement of lithium ion in the positive electrode. Fig. 1(a) illustrates the composite-NCM80 positive electrode active material present in the organic/inorganic composite SEs. It can be seen that an

amorphous layer for garnet type LLZAO material was formed on the surface of the composite-NCM80 obtained from the simultaneous co-precipitation method. Several LLZO synthesis studies confirmed that a single phase LLZO material was synthesized at a low calcination temperature [14, 35-38]. Xie et al reported the synthesis of garnet type LLZO at low temperature calcination process. A single phase LLZO material without an impurity was synthesized at 750 °C; it was measured that the ionic conductivity was 10^{-6} S cm^{-1} [35]. In addition, it was confirmed that small spherical nanoparticles are formed on the cathode material surface, which further confirms that a K_2NiF_4-type $La_2(Ni_{0.5}Li_{0.5})O_4$ material was mixed by residual lithium, Ni element from NCM80, and La elements from LLZAO material. A K_2NiF_4-type $La_2(Ni_{0.5}Li_{0.5})O_4$ material has a A_2BO_4 crystal structure, which exhibits better electrical conductivity than that of a perovskite ABO_3 crystal structure [39, 40]. P. Chosh et al reported that a $LiCoO_2$ cathode material was doped by La^{3+} to improve its structural stability. In addition, it was reported that as the doping amount of La^{3+} increased (La > 1.0 wt %), a perovskite-like $La_2(Li_{0.5}Co_{0.5})O_4$ material was produced. The electrical conductivity measurements showed that an La-doped $LiCoO_2$ cathode material (La > 1.0 wt %) exhibit a conventional semiconducting behavior and conductivity of approximately 1.1 x 10^{-3} S cm^{-1} at high temperatures, which improve the electrochemical performance [41]. These characteristics of ionic conductivity and electric conductivity improve the electrochemical performance of the composite-NCM80. These materials were examined under powder X-ray diffraction (XRD), field-emission scanning electron microscopy (FE-SEM), electrochemical impedance spectroscopy (EIS), and galvanostatic measurements.

Experimental

Material

Synthesis of NCM80 cathode material: $Ni_{0.8}Co_{0.1}Mn_{0.1}(OH)_2$ (NCM80) precursor synthesized using the co-precipitation method. The spherical precursor NCM80 was synthesized by a continuous-type co-precipitation method with LCTR-tera 3100 model equipment manufactured by Laminar Co., Ltd. An Ni-rich NCM811 aqueous solution consisting of $NiSO_4 \bullet 6H_2O$, $CoSO_4 \bullet 7H_2O$, and $MnSO_4 \bullet 5H_2O$ (molar ratio of Ni:Co:Mn =80:10:10) was gradually pumped into a 1 L continuous-type reactor, where a suitable amount of deionized water, NH_4OH, and NaOH solutions were filled without using an inert gas. Simultaneously, 4 mol/L each of NaOH solution (aq.) NH_4OH solution mixed with D.I water at a ratio of 1:1 (aq.), as chelating agents, were separately pumped into the reactor. An NCM80 aqueous solution and NH_4OH aqueous solution were pumped into the reactor at a flow rate of 2 ml/min and 0.5 ml/min, respectively. The NaOH aqueous solution pump was connected to the sensor that adjusted the flow rate according to the pH value. We set the pH value at 11 pH and maintained 4 h of residence time. The pH, flow rate, and precipitate morphology were checked every 4 h. The precursor powder $[Ni_{0.8}Co_{0.1}Mn_{0.1}](OH)_2$ was obtained after washing, filtering, and drying at 100 °C for 6 h. The dried powder was mixed with an Li source, and then, calcined at 500 °C for 10 h followed by calcination at 850 °C for 10 h in an O_2 atmosphere.

Composite-NCM80 cathode material: The spherical composite precursors $Ni_{0.8}Co_{0.1}Mn_{0.1}(OH)_2$ and $La_3Zr_2Al_{0.25}OH_x$ (NCM80-LZAOH) were synthesized using the continuous-type co-precipitation method with an LCTR-tera3100 system (Laminar Co., Ltd.). An NCM80-LZA aqueous solution consisting of $NiSO_4 \bullet 6H_2O$, $CoSO_4 \bullet 7H_2O$, $MnSO_4 \bullet 5H_2O$, $La(NO_3)_3 \bullet 6H_2O$, $ZrO(NO_3) \bullet xH_2O$, and $Al(NO_3)_3 \bullet 9H_2O$ (molar ratio of Ni:Co:Mn = 8:1:1, 0.5 wt% La:Zr:Al = 3:2:0.25) was gradually pumped into a 1 L continuous-type reactor, where a suitable amount of a D.I. water, NH_4OH, and NaOH solution was added without using an inert gas. Simultaneously, 4 mol/L NaOH solution (aq.) and NH_4OH solution mixed with D.I water at a ratio of 1:1 (aq.), as chelating agents, were separately pumped into the reactor. A composite-NCM80 aqueous solution and NH_4OH aqueous solution were pumped into the reactor at a flow rate of 2 ml/min and 0.5 ml/min, respectively. The NaOH aqueous solution pump was connected to the sensor that adjusted the flow rate according to the pH value. We set the pH value at 11 and maintained 4 h of residence time. The pH, flow rate, and precipitate morphology were checked every 4 h. The precursor powder was obtained after washing, filtering, and drying at 100 °C for 6 h. The dried powder (composite-NCM80 precursor) was calcined at 500 °C for 10 h, mixed with LiOH, and further calcined at 850 °C for 10 h in an O_2 atmosphere.

Structural and physical characterization

Powder X-ray Diffraction (XRD): The obtained powder of NCM80 and composite-NCM80 were analyzed using XRD with an X'pert Pro X-ray diffractometer (PANalytical) with Ni-filtered Cu Kα radiation (λ = 1.5406 Å), operating at 40 kV and 30 mA within a scanning angle, 2θ, and range of 10–80° using 0.01° steps. High Score Plus software was used to determine unit-cell parameters of the samples.

Ex-situ Powder X-ray Diffraction: The XRD analyses prior to electrochemical testing of the coin cell assembled by (NCM80 or composite-NCM80/LLZO-PEO-$LiClO_4$/Li-metal) were performed with a 9B high-resolution powder diffraction (HRPD) beamline at the Pohang accelerator laboratory (PAL)

Field Emission Electron Microscopy (FE-SEM): Particle morphologies and sizes were determined using FE-SEM. SEM images were obtained using an S-4700 instrument (HITACHI).

High Resolution Transmission Electron Microscope (HR-TEM & EDS mapping): The microstructure and elemental mappings of the samples were determined using TEM (TEM, TECNAI F20, Philips, Netherlands) at the Korean Basic Science Institute (KBSI, Gwangju Center) at 200 kV.

View Article Online DOI: 10.1039/D0TA07347D

X-ray Photoelectron Spectroscopy (XPS): The XPS measurements of the powder samples were performed using an angle-resolved X-ray photoelectron spectrometer (Theta Probe AR-XPS, Thermom Electron Corporation, UK) at the Korea Basic Science Institute (KBSI), Busan center, equipped with an MXR1 Gun-400 µm 15 keV spectrometer.

Potentiometric titration: The residual lithium present on the surface of the powder samples was analyzed using potentiometric titration (Metrohm) at 25 °C.

Raman Spectroscopy: The Raman measurement of the powder samples were performed using Raman microscope (Horiba Jobin-Yvon, France) at the Korean Basic Science Institute (KBSI, Gwangju Center).

Inductively coupled plasma atomic emission spectrometry (ICP-OES): The ICP-OES measurement of the powder samples were performed using Thermo Scientific iCAP 6300.

Electrochemical measurements

The electrochemical properties of the NCM80 and composite-NCM80 cathode material were examined using lithium metal as reference and counter electrodes. The active material (NCM80, composite-NCM80), SE (LLZO), conductive carbon (super P), and polyethylene oxide (PEO, M_v: 200,000) binder were used in a stoichiometric ratio of 70:5:5:20/75:0:5:20 to fabricate the electrode. The LLZO in the positive electrode improves the lithium ion conductivity of the electrode and provides a path for the movement of the lithium ions. The stoichiometrically mixed slurry was cast onto an Al foil and then dried at room temperature for approximately 12 h to form the cathode. We manufactured positive electrode with a loading weight of 5mg cm^{-2} and performed electrochemical evaluation by calculating the theoretical capacity of 170 mAh/g based on 1 C. A 2032 coin-type cell, consisting of the cathode (14φ) and lithium-metal anode (16φ) separated by the composite membrane sheet (19φ), was synthesized as previously described (fabricated in a dry room and aged for 12 h prior to the electrochemical experiment). The charge–discharge measurements of the synthesized coin-type cell were performed at the potential range from 2.5 to 4.0 V vs. Li^0/Li^+ at different current densities using Wonatech WBCS 3000L.

Electrochemical impedance spectroscopy (EIS) was conducted at room temperature using a Bio-Logic Science instrument (SP-240) to determine variations in resistance in the assembled coin cell. The cell was tested at the first and 50th cycles and examined at each cycle for 100 mHz–1.0 MHz frequency range at 70 °C.

Results and discussion

Fig. 2 shows the primary diffraction peaks of the XRD patterns of the NCM80 and composite-NCM80 cathode material. The patterns shown in Fig. 2(a) are indexed to a hexagonal structure (space group: R3-m). However, between 20° and 35°, there are four minor peaks, as shown Fig. 2(b), that can been found in the composite-NCM80 cathode material, which are indexed to the $La_2(Ni_{0.5}Li_{0.5})O_4$ (space group: I4/mmm) with the K_2NiF_4 type structure. During the calcination at high-temperature, Ni ion present on the surface of the NCM80 and La ion obtained from the LZAO precursor combined with the residual lithium materials, thus forming the $La_2(Ni_{0.5}Li_{0.5})O_4$ material. The K_2NiF_4-type $La_2(Ni_{0.5}Li_{0.5})O_4$ material has a A_2BO_4 crystal structure, which exhibits better electrical conductivity than the perovskite ABO_3 crystal structure [40]. P. Chosh et al reported a $LiCoO_2$ cathode material that was doped by La^{3+} to improve structural stability. In addition, it was reported that the doping amount of La^{3+} increased (La > 1.0 wt %), and a perovskite-like $La_2(Li_{0.5}Co_{0.5})O_4$ material was produced. The electrical conductivity measurements showed that the La-doped samples exhibit a conventional semiconducting behavior and conductivity of approximately 1.1 x 10^{-3} S cm^{-1} at a high temperature, which contribute to improve the electrochemical performance [41]. Fig. 2(c) and (d) show that (003) and (104) peaks, which are the representative peaks of layered structure, of composite-NCM80 shifted to the left when compared with those of the NCM80 because of the large size La^{3+} that are doped on the NCM80 [40].

According to the Rietveld refinement result in Table 1 showing larger lattice parameter, c/a ratio, and R-factor of $I_{(003)}/I_{(104)}$ ratio of the composite-NCM80 than those of the NCM80 indicating that the large size La^{3+} ions have been doped into the layered lattice during the calcination at high temperatures. These results are associated with the XRD pattern of the $I_{(003)}$ and $I_{(104)}$ peaks and indicated that certain La^{3+} ions that were in the coated LLZAO were doped during the calcination at high temperatures. The c/3a ratio and $I_{(003)}/I_{(104)}$ ratio have been reported to be an indication of cation ordering of the layered structure cathode materials. For a pure hexagonal closed packed structure, where the Ni and Li atoms are disordered, the value of c/3a is 1.633; a greater c/3a ratio suggests a more ordered structure. Then, the intensity ratio called the R-factor of the $I_{(003)}/I_{(104)}$ represents the degree of cation disorder for Ni-based cathode material due to similar ionic radius of Ni^{2+} (0.69 Å) and Li^+ (0.76 Å) cause the cation mixing during the Li^+ intercalation/deintercalation. When the R-factor is lower than 1.2, the Ni^{2+} ions occupy the Li^+ ion site, which indicates that the material shows a poor electrochemical characteristic [34].

The potentiometric titration experiment was conducted to confirm the effect of the K_2NiF_4 type $La_2(Ni_{0.5}Li_{0.5})O_4$ material on the reduction of residual lithium compounds of Li_2CO_3 and LiOH on the surface of NCM80 and composite-NCM80. the corresponding results are shown in Table 2. In the composite-NCM80 sample, the amount of residual lithium compounds of Li_2CO_3 and LiOH present on the surface of the cathode material is significantly reduced when compared with that of the NCM80. The $La_2(Ni_{0.5}Li_{0.5})O_4$ material is present in the impurity phase of the NCM80 material, but it plays a role in removing residual lithium on the cathode material surface. It may improve the electrochemical properties of the composite-NCM80.

The morphology and homogenous distribution of the NCM80 and composite-NCM80 material were investigated using FE-SEM (Fig. 3 (a), (b)); the SEM images show a spherical shape and

View Article Online
DOI: 10.1039/D0TA07747D

an almost equal primary and secondary particles size with a diameter of less than 5 µm. The FE-TEM images under low and high magnification were procured to gain further insight into the crystallographic characteristics of the NCM80 and composite-NCM80 samples, as shown in Fig. 3 (c) and (d). It was confirmed that the primary particles of 100–200 nm were aggregated in the NCM80 and composite-NCM80. Fig 3 (c) images show the characteristic crystal plane of the $Li(Ni_{0.8}Co_{0.1}Mn_{0.1})O_2$ layered structure, and the calculated planes were similar to those of the XRD patterns. An interplanar distance of 0.23 nm, calculated from the highly magnified images, corresponds to the (012) plane. This demonstrates that the NCM80 material was synthesized well using the co-precipitation method. Fig 3 (d) shows the TEM images of the composite-NCM80 samples and indicated an interplanar distance of 0.47 nm, which corresponds to the (003) plane. However, unlike the surface of the NCM80, the primary particles of the composite-NCM80 appear as a uniformly coating layer of approximately 10 nm (Fig 3 (d) right). In addition, it can be confirmed that small nanoparticles with a size of 1–2 nm exist on the material surface. The interplanar distance of the nanoparticles was calculated to be 0.283 nm, which correspond to the (103) plane of the $La_2(Ni_{0.5}Li_{0.5})O_4$ material.

Elemental mapping using the EDS was performed to investigate the distribution of chemical elements in the NCM80 and composite-NCM80; the corresponding results are shown in Fig. 4. Fig. 4 (a) and (b) indicate that the Ni, Co, and Mn and Ni, Co, Mn, La, Zr, and Al elements, respectively, are uniformly distributed on the material surface, which indicate that the LLZAO material coating was present uniformly. In the XRD analysis of the composite-NCM80 material, the LLZAO peak present in the material could not be found owing to the low content of LLZAO material. However, through the EDS analysis, the LLZAO material surfaced indirectly through the La, Zr, and Al elements present evenly on the surface.

In addition, the inductively coupled plasma optical emission spectrometry results in Table 3 reveal that the experimental and theoretical atomic contents of the NCM80 and composite-NCM80 material. The amount of La, Zr and Al in the composite-NCM80 material total 0.5 wt%, which agrees well with the theoretical value. Therefore, this result confirmed that the composite-NCM80 material of the elements synthesized by the simultaneous co-precipitation reaction of the two materials are uniformly distributed.

To confirm the crystalline structure of composite-NCM80 cathode material, Raman spectroscopy was investigated and as shown in Fig. 5. To obtain spectrum information of LLZAO and NCM80 include in the composite-NCM80 sample, NCM80, composite-NCM80 and LLZAO (TOSIMA) material were proceed. In the case of composite-NCM80, the peak about 550 cm^{-1} was confirmed to NCM80 sample signal [42]. The peak appearing at 100 -150 cm^{-1} is associated with La cation vibration and the peak about 640 cm^{-1} is result of stretching the Zr-O bond [43, 44]. Although the signal was weak, it was confirmed the peak of LLZAO also appeared. Although the XRD pattern was not confirmed LLZAO material in the composite-NCM80, Raman spectroscopy result indicated that LLZAO and NCM80 were mixed and the layer present on the composite-NCM80 surface is amorphous LLZAO layer.

The XPS analysis of the NCM80 and composite-NCM80 material was performed to investigate the effect of the $La_2(Ni_{0.5}Li_{0.5})O_4$ material on the NCM80, as shown in Fig. 6. The figure shows the XPS peaks for the Ni (2p) of the NCM80 and composite-NCM80 materials, and the $Ni2p_{3/2}$ peaks show the chemical states of the Ni^{2+} and Ni^{3+} ions at 853.6 and 855.7 eV, respectively. In the composite-NCM80 sample, the XPS spectrum revealed that the intensity ratio obtained for the peaks of the Ni^{2+} and Ni^{3+} ions increased when compared with that of the NCM80. This is because of $La_2(Ni_{0.5}Li_{0.5})O_4$; Ni forms a +3 valance ions on the surface of the NCM80 by combining with La from the LZAO precursor and Ni from NCM80 during high-temperature calcination. This increased the Ni^{3+} contribution in reducing the degree of Ni^{2+}/Li^+ mixing during the synthesis, which is similar to the Rietveld refinement result shown in Table 1.

Fig. 7 and Fig. 8 present the electrochemical properties of the NCM80 and composite-NCM80 electrodes vs. Li^0/Li^+. All positive electrodes were measured in a potential window range 2.5–4.0 V at 70 °C temperature. To eliminate negative effects on the PEO binders in the positive electrode, the Li^+ ion had to be extracted from the NCM80 and composite-NCM80 electrodes at less than 4.0 V vs. Li^0/Li^+ owing to the restricted stability of the PEO binder in the ASSB, which cannot exceed 4.0 V vs Li^0/Li^+. In the case of LIBs system using a liquid electrolytes, lithium ions move freely through the fluid. But in ASSBs, LLZO solid electrolyte was added into the positive electrode to increase lithium ion mobility because lithium ion moves in the lattice. Fig. 7 demonstrates the electrochemical performance of the NCM80 and composite-NCM80 positive electrodes synthesized by mixing the active material, conductive material, LLZO SE, and binder at a ratio of 70:5:5:20. Fig. 7 (a) shows the initial charge/discharge curves of the NCM80 and composite-NCM80 samples measured at 0.1 C (1 C = 170 mAh) and indicates their initial discharge capacity of 138.17 and 143.51 mAh/g, respectively, and coulombic efficiency of 90.82 and 91.41 %, respectively. In the composite-NCM80 sample, initial discharge capacity is higher than that of the NCM80 due to the high ionic conductivity of the LLZAO material attached to the NCM80 surface, which improves the lithium ion diffusion between the cathode material and SE in the positive electrode [34]. Further since the $La_2(Ni_{0.5}Li_{0.5})O_4$ material present as a nanoparticles on the cathode material surface contribute to increasing electric conductivity, it seem to be contribute to the increase initial capacity of composite-NCM80. Fig. 7 (b) shows the cyclability of the NCM80 and composite-NCM80 electrodes determined at a rate of 0.2 C in the 2.5–4.0 V potential window at 70 C during 50 cycles. After 50 cycles, the composite-NCM80 material shows higher discharge capacity retention of 83.79% than that of the NCM80 (77.45 %). The rate performance of the NCM80 and composite-NCM80 material are presented in Fig. 7 (c) and (d). It shows that the difference in discharge capacity between the NCM80 and composite-NCM80 does not appear at a low current density of 0.1 (and 0.2 C. However, as the current rate increases

at 0.5 C, the capacity retention ratio of the two electrodes show a large difference. In the NCM80 sample, the discharge capacity retention rate is shown to be approximately 50 %. However, in the composite-NCM80 sample, the discharge capacity retention was 63% which shows better discharge capacity retention, with an increase in the current rate, than that of the NCM80.

In ASSBs, the SE present in the positive electrode efficiently moves the lithium ions from the positive electrode to the anode similar to an organic liquid electrolyte. To confirm the electrochemical properties according to the absence of the SE in the positive electrode, the ratio of active material, SE, conductive material and binder was changed to 75:0:5:20, as shown in Fig. 8. Fig. 8 (a) shows the initial charge/discharge curves of the NCM80 and composite-NCM80 samples. The NCM80 sample shows a discharge capacity of 137.71 mAh/g, which is similar to that of the previous composition (70:5:5:20) shown in Fig. 7 (a). However, the composite-NCM80 sample shows an increased discharge capacity of 151.50 mAh/g when compared with the previous ratio (70:5:5:20). Fig. 8 (a) indicates the cyclability of the NCM80 and composite-NCM80 determined at a rate of 0.2 C during 50 cycles. After 50 cycles, the composite-NCM80 material exhibited higher discharge capacity retention of 87.99% than that of the NCM80 (82.06%), similar to the previous ratio shown Fig. 7 (b). These results are associated with preventing a side reaction at the cathode material surface, which occurs as the charge/discharge proceeds, because it reduces the residual lithium compound present on the cathode surface as a nanoparticles. To identify the rate capability of the NCM80 and composite-NCM80 were performed by applying various current densities from 0.1 to 0.5 C, as shown in Fig. 8 (c) and (d). The discharge capacity retention of the NCM80 and composite-NCM80 decreased with an increase in the charge/discharge current while that of the composite-NCM80 decreased gradually. The discharge capacity retention of the composite-NCM80 at 0.1, 0.2, and 0.5 are 100, 97.87, and 73.98%, respectively, which are higher than those of the NCM80 (100, 91.41, and 36.62%). The composite-NCM80 exhibits a better rate performance because of the Li^+ ion conductor layer on the surface, and an appropriate La^{3+} ion doing effect of the composite-NCM80 can effectively maintain the structural stability [36]. Moreover, since the $La_2(Ni_{0.5}Li_{0.5})O_4$ material present as nanoparticles on the cathode material surface act an electric conductor, it can be confirmed that the rate capability is improved without solid electrolyte in the positive electrode [41].

To further understand the effect of the $La_2(Ni_{0.5}Li_{0.5})O_4$ nanoparticles on the cathode surface during the cycling in an assembled coin cell, the EIS was performed at 70 °C. Fig 8 shows the EIS spectra of the assembled coin cell (Al/NCM80 or composite-NCM80//PEO-LLZO-$LiClO_4$-//Li-metal) recorded at the 100 mHz – 1 MHz range, for the first cycle and 50th cycle. The Nyquist plots show conventional semicircles at high and medium frequencies and an inclined line in the low-frequency region that corresponds to the interfacial resistance associated with the lithium-ion diffusion in the bulk material. R_b, R_s, and R_{ct} represent the bulk resistance of the cell (electrolyte and electrode, R_b), interfacial resistance (R_s), and charge transfer resistance (R_{ct}). The lithium-ion diffusion through the interface between the cathode and SE (R_s) is reflected in the first semicircle. The second semicircle is associated with charge-transfer resistance (R_{ct}) [45]. The measured impedance spectra were quantitatively analyzed using the equivalent circuit in Fig. 9 (c). In the equivalent circuit, R_1 represents contact resistance; R_2 and CPE_2, the resistance and the constant phase element for surface films; R_3 and CPE_3, the charge-transfer resistance and the constant phase element for double-layer charging/discharging; and Z_d represents the diffusion impedance. The resistance parameters obtained from the fitting analysis are summarized in Table 4. The impedance result reveal that the electrochemical properties of the ASSBs strongly depend on the cathode material used, as evidence by significantly reduced impedance of the cell with composite-NCM80 material. This result indicates that the $La_2(Ni_{0.5}Li_{0.5})O_4$ nanoparticles on the NCM80 cathode surface with the electric conductivity contribute in reducing the resistance at the interface between the cathode and SE. As a result, it can be confirmed that the composite-NCM80 sample shows better electrochemical properties.

To further explore the performance attenuation mechanism, XRD analysis was performed on the electrodes of the NCM80 and composite-NCM80 after 1 and 50 cycles at 0.2 C at 70 °C, as shown in Fig. 10. We assemble the coin cell for ASSB with the structure shown in Fig. 1 (a). The coin cell for Ex-situ XRD analysis was designed to drill holes in the center of cap, case and spacer to pass through the electric beam. The XRD pattern is a mixture of the NCM80 and LLZO material from the positive electrode and solid electrolyte sheet, and the corresponding information of the pattern can be found in references (ICSD-98-016-9367, ICSD-98-042-2259). In Fig. 10 (a) and (b), the LLZO peaks from the solid electrolyte sheet in the two samples indexed cubic structure and no peak shift, respectively. The diffraction peak intensity of the NCM80 weakened after 50 cycles at 0.2 C, where the peak intensity of the (003) lattice facet of the NCM80 reduced by 89.80%. However, the peak intensity of each characteristic peak in the composite-NCM80 was maintained and intensity of the (003) lattice facet was maintained at 93.39%, while that of the (101) and (104) crystal lattices was maintained at 98.49% and 91.16% when compared with the 93.36 and 82.01%, respectively. Generally, the layered structure cathode material where cycled in a region of 4.2 V or higher, structural changes tend to be severe due to the expansion of the C-axis owing to the lithium intercalation/de-intercalation [46]. However, in the ASSB using PEO binder, its potential window is limited up to 4.0 V because of the structural stability of the PEO binder during cycling. Further, as the cyclability was tested at a low potential window, the two samples may maintain a high intensity retention of greater than 90% after 50 cycles. These results demonstrate a great cycle stability of the composite-NCM80, as shown in Fig. 7 (b).

Conclusions

In summary, we investigated a composite-NCN80 cathode material to use in all-solid-state lithium ion batteries with an

oxide-based SE. XRD patterns of NCM80 and composite-NCM80 are indexed to a hexagonal structure, respectively. However, for the 20°–35° region, K_2NiF_4-type structure of $La_2(Ni_{0.5}Li_{0.5})O_4$ material is indexed. Further, the potentiometric titration result shows that the ratio of residual lithium on the cathode material surface of the composite-NCM80 decreases when compared with that of the NCM80. During the calcination at high-temperature, the Ni ion present on the surface of the NCM80 and La ion from the LZAOH precursor combined with the residual lithium materials, forming the $La_2(Ni_{0.5}Li_{0.5})O_4$ material. In the composite-NCM80 samples, the electrochemical performance improved when compared with that of the NCM80 samples because $La_2(Ni_{0.5}Li_{0.5})O_4$, which exists as a spherical nanoparticle on the surface of the cathode material, facilitates the movement of lithium ions in the interface between the SE and cathode material within the positive electrode due to their high electric conductivity.

Conflicts of interest

In accordance with our policy on Conflicts of interest please ensure that a conflicts of interest statement is included in your manuscript here. Please note that this statement is required for all submitted manuscripts. If no conflicts exist, please state that "There are no conflicts to declare".

Acknowledgements

This work was supported by the Technology Development Program of the National Research Foundation (NRF). This work is funded by the Ministry of Science, ICT and Future Planning (NRF-2018M1A2A2063336 & 2017M3A7B4049173).

References

1 Y. H. Cho, D, H, Jang, J. B. Yoon, H. C. Kim, T. K. Ahn, K. W. Nam, Y. E. Sung, W. S. Kim, Y. S. Lee, X. Q. Yang and W. S. Yoon, *J. Alloy and Compd.*, 2013**, 562,** 219–223.
2 M. Armand and J. M. Tarascon, *Nature*, 2008, **451**, 652–657.
3 X. Zhan, S. Gao and Y. T. Cheng, *Electrochim. Acta*, 2019, **300**, 36–44.
4 D. Y. Oh, Y. J. Nam, K. H. Park, S. H. Jung, S. J. Cho, Y. K. Kim, Y. G. Lee, S. Y. Lee and Y. S. Jung, *Adv. Energy Mater.*, 2015, **5**, 1500865.
5 A. Gurung, J. Pokharel, A. Baniya, R. Pathak, K. Chen, B. S. Lamsal, N. Ghimire, W.H. Zhang, Y. Zhou and Q. Qiao, *Sustain. Energy Fuels*, 2019, **3**, 3279–3309.
6 R. Koerver, I. Aygun, T. Leichtweiß, C.Dietrich, W. Zhang, J. O. Binder, P. Hartmann, W. G. Zeier and J. Janek, *Chem. Mater.*, 2017, **29**, 5574–5582.
7 S. J. Choi, S. H. Choi, A, D. Bui, Y. J. Lee, S. M. Lee, H. C. Shin and Y. C. Ha, *ACS Appl. Mater. Interfaces*, 2018, **10**, 31404–31412.
8 Y. Kato, R. Saito, M. Sakano, A. Mitsui, M. Hirayama and R. Kanno, *J. Power Sources*, 2014, **271**, 60–64.
9 W. J. Li, M. Hirayama, K. Suzuki and R. Kanno, *Solid State Ionics*, 2016, **285**, 136–142.
10 M. Monchak, T. Hupfer, A. Senyshyn, H. Boysen, D. Chernyshov, T. Hansen, K. G. Schell, E. C. Bucharsky, M. J. Hoffmann and H. Ehrenberg, *Inorg. Chem*. 2016, **55**, 2941−2945.
11 S. Yu, S. Schmohl, Z. Liu, M. Hoffmeyer, N. Schon, F. Hausen, H. Tempel, H. Kungl, H. D. Wiemhofer and R. A. Eichel, *J. Mater. Chem. A*, 2019, **7**, 3882–3894.
12 Y. F. Deng, S. X. Zhao, Y. H. Xu and C. W. Nan, *J. Mater. Chem. A,* 2014, **2,** 18889–18897.
13 W. J. Kwon, H. I. Kim, K. N. Jung, W. S. Cho, S. H. Kim, J. W. Lee and M. S. Park, *J. Mater. Chem. A*, 2017, **5**, 6257–6262.
14 K. W. Kim, S. H. Yang, M. Y. Kim, M. S. Lee, J. S. Lin, D. R. Chang and H. S. Kim, *J. Ind. Eng. Chem*. 2016, **36**, 279–283.
15 D. O. Shin, K. B. Oh, K. M. Kim, K. Y. Park, B. J. Lee, Y. G. Lee and K. S. Kang, *Sci. Rep*. 2015, **1**, 8053.
16 T. Thompson, J. Wolfenstine, J. L. Allen, M. Johannes, A. Huq, I. N. David and J. Sakanoto, *J. Mater. Chem. A*, 2014, **2**, 13431–13436.
17 X. Ban, W, Zhang, N. Chen and C. Sun, *J. Phys. Chem. C*, 2018, **122**, 9852−9858.
18 F. Croce, G.B. Appetecchi, L. Persi and B. Scrosati, *Nature*, 1998, **394**, 456–458.
19 D. H. Kim,M. Y. Kim, S. H. Yang, H. M. Ryu, H. Y. Jung. H. J. Ban, S. J. Park, J. S. Lim and H. S. Kim, *J. Ind. Eng. Chem.,* 2019**, 71,** 445–451.
20 K. Nie, Y. Hong, J. Qiu, Q. Li, X. Yu, H. Li and L. Chen, *Front, Chem*., 2018, **616.**
21 L. Xu, S. Tang, Y. Cheng, K. Wang, J. Liang, C. Liu, Y. C. Cao, F. Wei and L. Mai, *Joule*, 2018, **10**, 1991-2015.
22 S. Ohta, S. Komagata, J. Seki, T. Saeki, S. Morishita and T. Asaoka, *J. Power Sources*, 2013, **238,** 53-56.
23 H. Chen, Q. Y. Liu, M. X. Jing, F. Chen, W. Y. Yuan, B. W. Ju, F. Y. Tu, X. Q. Shen and S. B. Qin, *ACS appl. Mater. Interfaces*, **2020**, 12, 15120-15127.
24 H. Wakayama, H, Yonekura and Y. Kawai, *Chem. Mater.* **2016**, 28, 4453-4459.
25 Y. Seino, Y. Ota and K. Takada, *J. Power Sources*, **2011**, 196, 6488-6492.
26 Z. Jiang, B. Carroll and K. M. Abraham, *Electrochim. Acta*, 1997, **42**, 2667–2677.
27 P. Raghavan, J. Manuel, X. Zhao, D.S. Kim, J.H. Ahn and C. Nah, *J. Power Sources*, 2011, **196**, 6742–6749.
28 H.S. Jeong, D.W. Kim, Y.U. Jeong and S.Y. Lee, *J. Power Sources*, 2010, **195**, 6116–6121.
29 D. Zhang, L. Zhang, K. Yang, H. Wang, C. Yu, D. Xu, B. Xu and L. M. Wang, *ACS Appl. Mater. Interfaces*, 2017, **9**, 36886–36896.
30 F. Hao, F. Han, Y. Liang, C. Wang and Y. Yao, *Mater. Res. Bull*, 2018, **43**, 775–781.
31 F. Strauss, T. Vartsch, L. D. Biasi, A. Y. Kim, J. Janek, P. Hartmann and T. Brezesinski, *ACS Energy Lett.* 2018, **3**, 992−996.
32 F. Han, J. Yue, C. Chen, N. Zhao, X. Fan, Z. Ma, T. Gao, F. Wang, X. Guo and C. Wang, *Joule,* 2018, **2**, 497–508.
33 A.Y. Kim, F. Strauss, T. Bartsch, J. H. Teo, T. Hatsukade, A. Mazilkin, J. Janek, P. Hartmann and T. Brezesinski, *Chem. Mater.*, 2019, **31**, 9664−9672
34 K. J. Heo, J. S. Lee, H. S. Kim, M. Y. Kim, H. J. Jeong, J. K. Kim and J. S. Lim, J. *Electrochem. Soc*., 2018, **165**, A2955–A2960.
35 H. Xie, Y. Li and J. Goodenough, *Mater. Res. Bull.,* 2012, **47**, 1229–1232.
36 C. Shao, H. Liu, Z. Yu, Z. Zheng, Z. N. Sun and C. Diao, *Solid State Ionics*, 2016, **287**, 13–16.

37 S. Afyon, F. Krumeich and J. L. M. Rupp, *J. Mater. Chem. A*, 2015, **3**, 18636–18648.
38 Z. Hu, H. Liu, H. Ruan, R. Hu, Y. Su and L. Zhang, *Ceram. Int.,* 2016, **42**, 12156–12160.
39 M. Sayer and P. Odier, *J. Solid State Chem*., 1987, **67**, 26–36.
40 F. Wu, Q. Li, L. Chen, Q. Zhang, Z. Wang, Y. Lu, L. Bao, S. Chen and Y. Su, *ACS Appl. Mater. Interfaces,* 2019, **11**, 36751−36762.
41 P. Ghosh, S. Mahanty and R. N. Basu, *Electrochim. Acta*, 2009, **54**, 1654–1661.
42 E. Flores, P. Novak and E. J. Berg, *Front. Energy Res*., 2018, **6**.
43 K. B. Dermenci and S. Truan, *Int. J. Energy Res.*, 2019, **43**, 141-149.
44 G. Larraz, A. Orera and M. L. Sanjuan, *J. Mater. Chem. A*, 2013, **1**, 11419.
45 W. S. Choi, H. C. Shin, J. M. Kim, J. Y. Choi and W. S. Yoon*, J. Electrochem. Sci. Technol*., 2020, **11**, 1–13.
46 Y. Kobayashi, M. Tabuchi, H. Miyashiro and N. Kuriyama *J. Power Sources,* 2017, **364,** 156–162.

Tables

Table 1. Lattice parameter of NCM80 and compsite-NCM80.

Table 2. Titration results of residual lithium for NCM80 and composite-NCM80.

Table 3. ICP analysis of NCM80 and composite-NCM80 cathode material showing the elements Ni, Co, Mn, La, Zr, and Al.

Table 4. Resistance parameters of coin cell with NCM80 and composite-NCM80 cathode material after 1st and 50th cycles, determined from the fitting of the impedance spectra to the equivalent circuit (Fig. 8).

Captions for Figures

Fig. 1. Schematic diagram of (a) all-solid-state battery system of positive electrode for composite-NCM80, (b) TEM image of composite-NCM80, and (c) Rate capability determined at 70 °C for various current densities of 0.1–0.5 C.

Fig. 2. Powder X-ray diffraction patterns of (a) NCM80 and composite-NCM80 cathode material. (b) XRD pattern 20°–35° of $La_2(Ni_{0.5}Li_{0.5})O_4$ material region. (c) I_{003} peak of NCM80 and composite-NCM80. (d) I_{104} peak of NCM80 and composite-NCM80.

Fig. 3. SEM images of (a) NCM80 (b) composite-NCM80 samples, and TEM images of (c) NCM80 and (d) composite-NCM80

Fig. 4. EDS mapping images of (a) NCM80 showing distribution of Ni (green), Co (red), Mn (blue), and (b) composite-NCM80 showing distribution of Ni (green), La (yellow), Zr (pink), and Al (white).

Fig. 5. Raman spectra of cubic structure LLZAO (TOSIMA), NCM80 and composite-NCM80 cathode material.

Fig. 6. XPS spectra for Ni 2p of (a) NCM80 and (b) composite-NCM80. Black line represents the experimental data while the other lines represent the fitting result.

View Article Online
DOI: 10.1039/D0TA07345D

Fig. 7. Electrochemical performance of NCM80 and composite-NCM80 assembled 2032 coin-cell and the ratio of active material:solid electrolyte:conductive material:binder = 70:5:5:20) in the positive electrode. (a) Initial charge/discharge curves of 0.1 C at 70 °C. (b) Cycle performance of more than 50 cycles of 0.2 C at 70 °C. Rate capability determined at 70 °C for various current densities of 0.1–0.5 C for (c) discharge capacity and (d) discharge capacity retention.

Fig 8. Electrochemical performance of NCM80 and composite-NCM80 assembled 2032 coin-cell and the ratio of active material:solid electrolyte:conductive material:binder = 75:0:5:20) in the positive electrode. (a) Initial charge/discharge curves of 0.1 C at 70 °C. (b) Cycle performance of more than 50 cycles of 0.2 C at 70 °C. Rate capability determined at 70 °C for various current densities of 0.1–0.5 C for (c) discharge capacity and (d) discharge capacity retention.

Fig. 9. EIS spectra of assembled coin cells (Al/NCM80 or composite-NCM80/PEO-LiClO4-LLZO/Li metal) recorded over the 100 mHz–1 MHz range for (a) NCM80 and composite-NCM80 electrode at 1st cycle, and (b) NCM80 and composite-NCM80 electrode at 50th cycles. (c) Equivalent circuit used for fitting of the measured impedance data. *R, CPE,* and Z_d represent the resistance, constant phase element, and diffusion impedance, respectively.

Fig. 10. Ex-situ X-ray diffraction pattern of assembled 2032 coin cells (Al/NCM80 or Composite-NCM80/LLZO-PEO-LiClO4/Li metal) of 1st cycle and 50th cycle (a) NCM80 and (b) composite-NCM80.

View Article Online
DOI: 10.1039/D0TA07347D

Fig 1

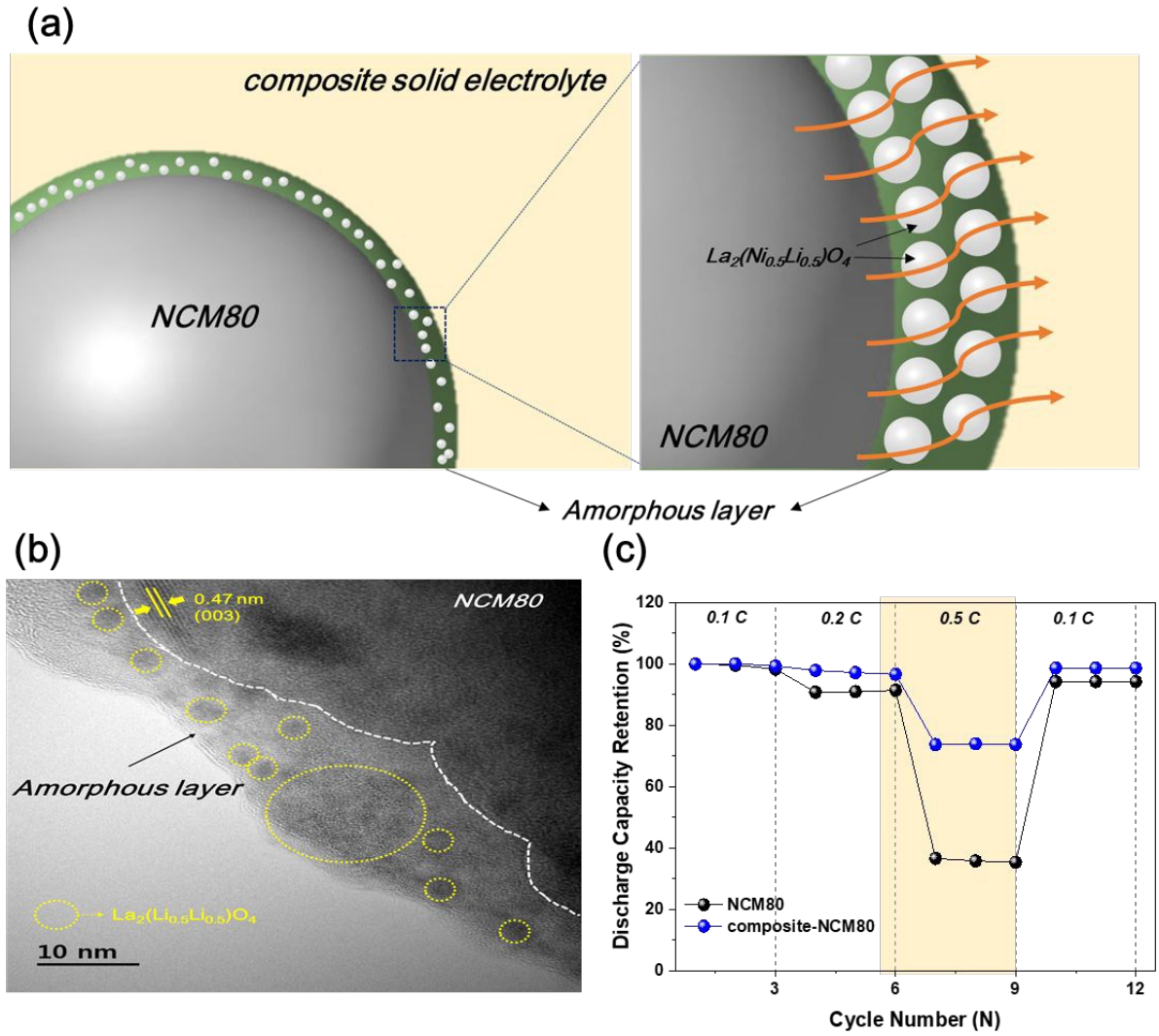

View Article Online
DOI: 10.1039/D0TA07347D

Fig 2

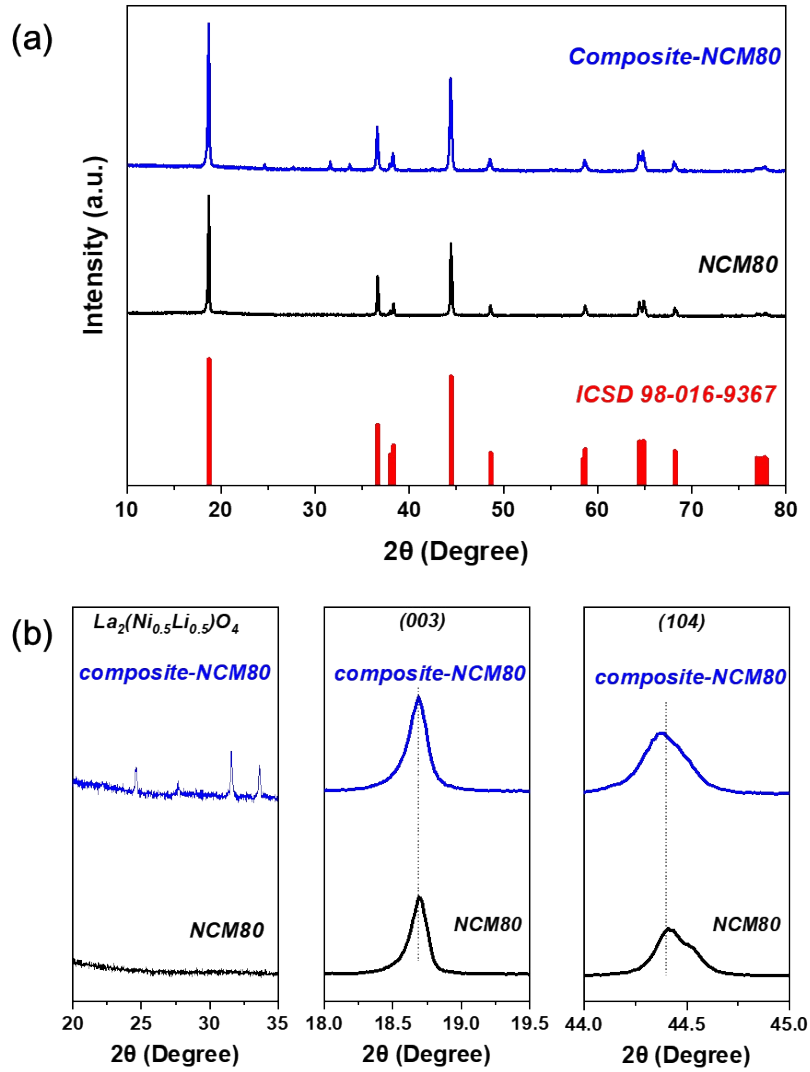

View Article Online
DOI: 10.1039/D0TA07347D

Fig 3

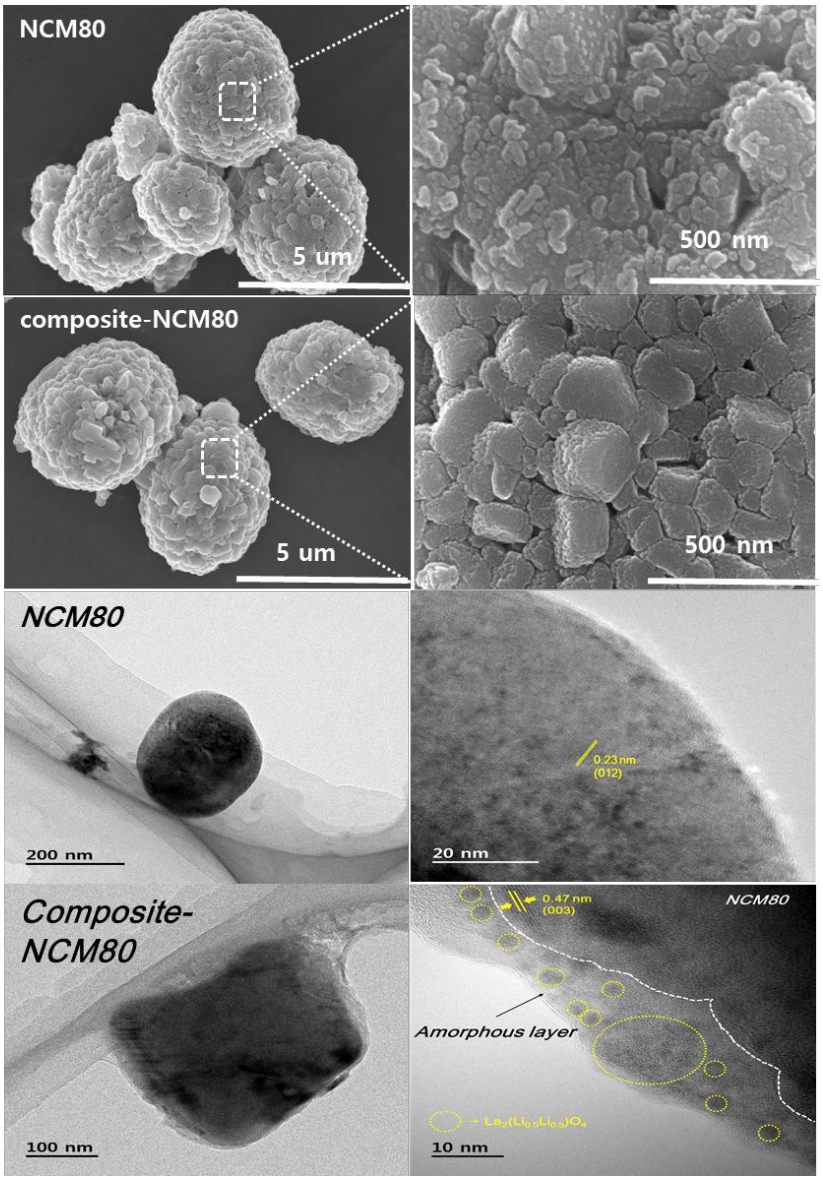

View Article Online
DOI: 10.1039/D0TA07347D

Fig 4

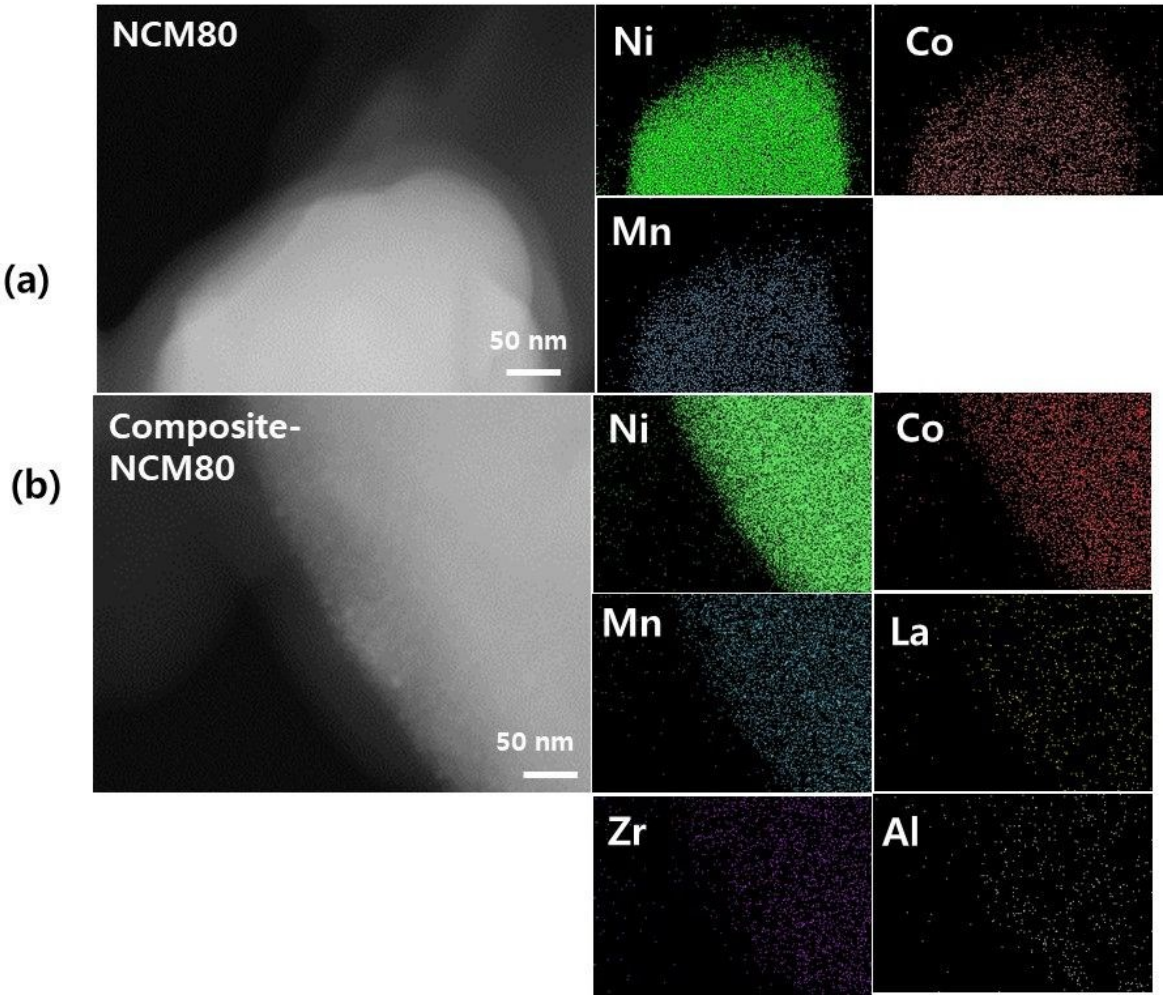

View Article Online
DOI: 10.1039/D0TA07347D

Fig 5

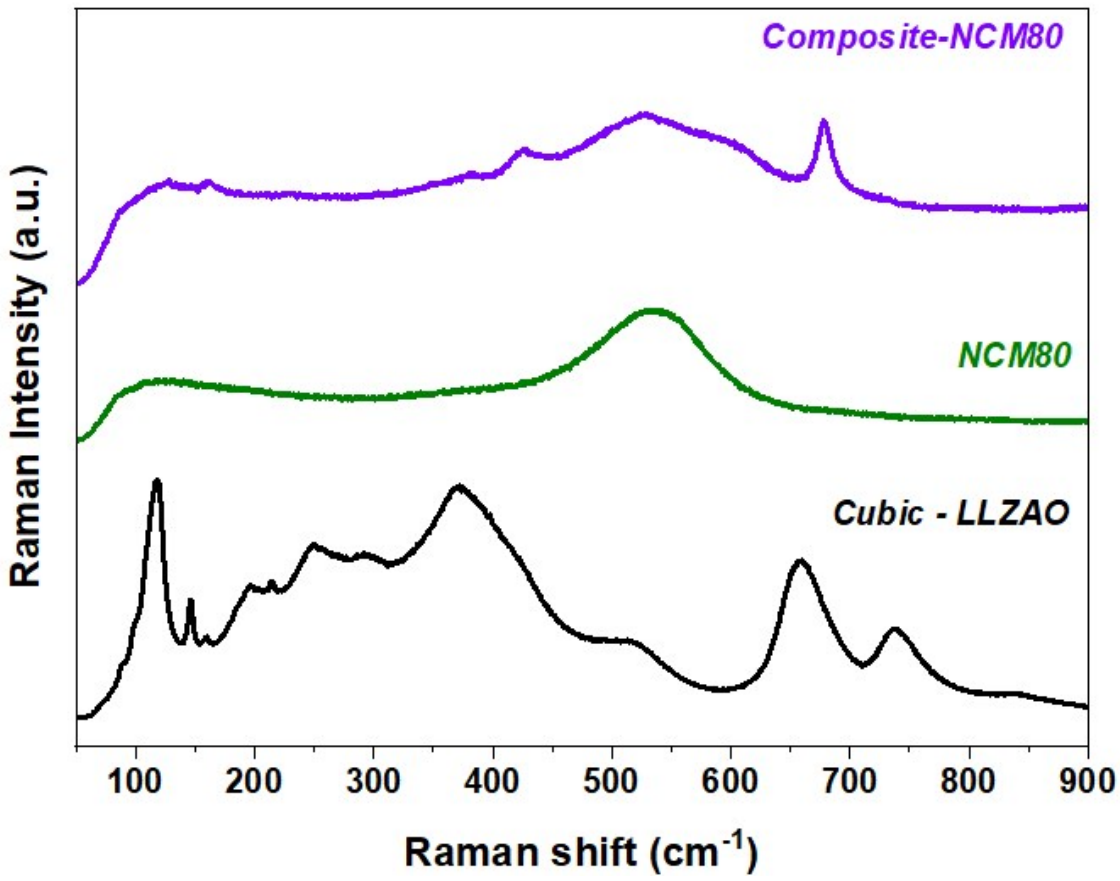

View Article Online
DOI: 10.1039/D0TA07347D

Fig 6

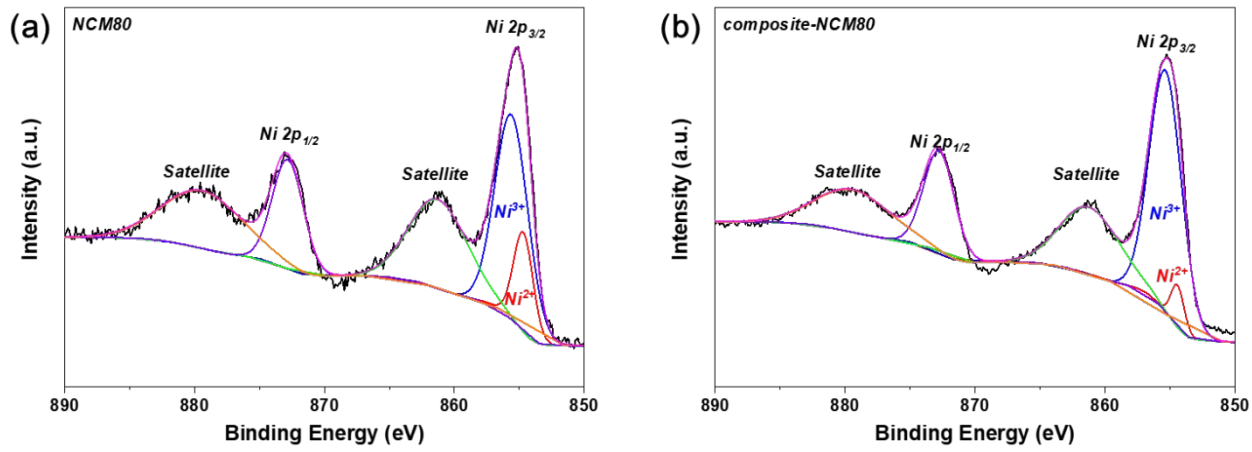

View Article Online
DOI: 10.1039/D0TA07347D

Fig 7

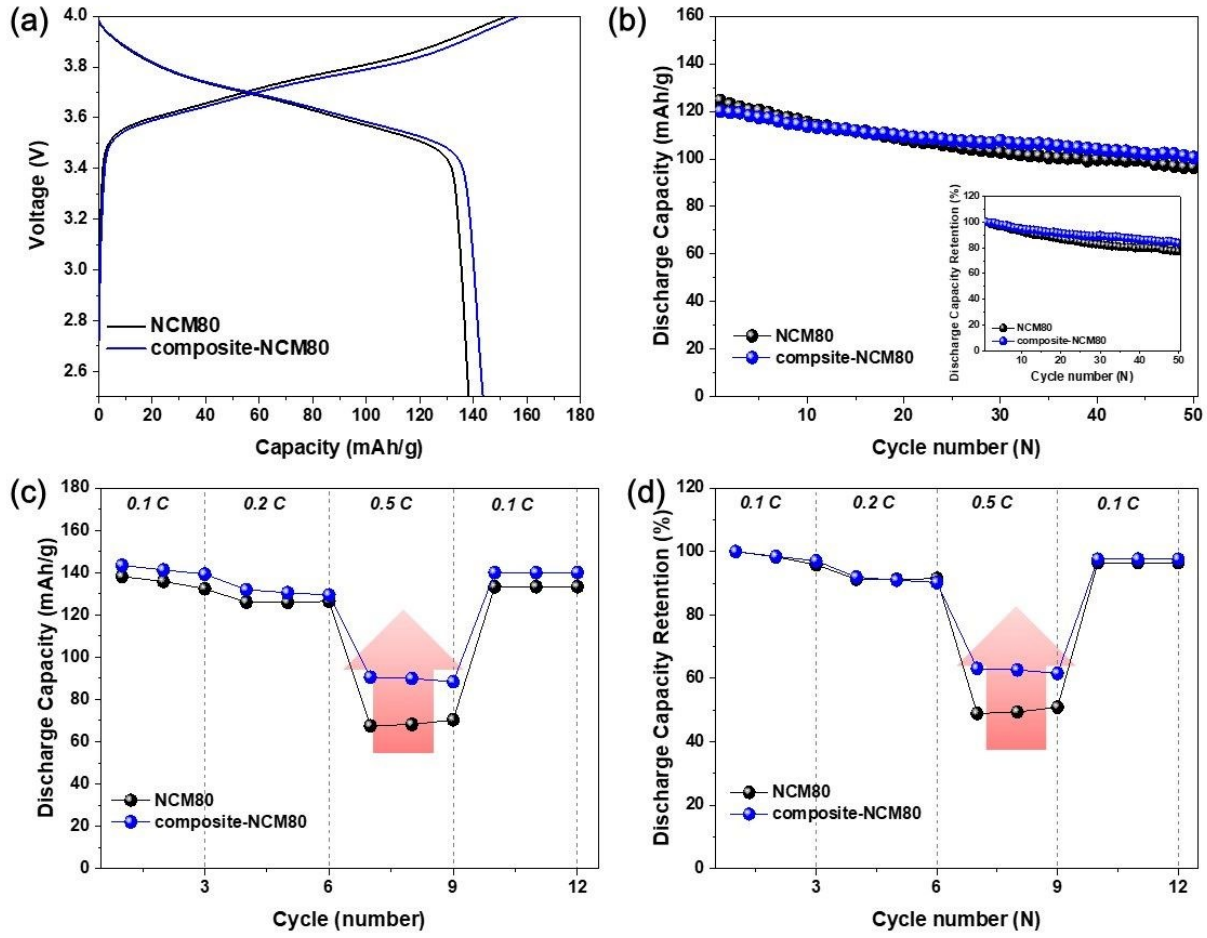

View Article Online
DOI: 10.1039/D0TA07347D

Fig 8

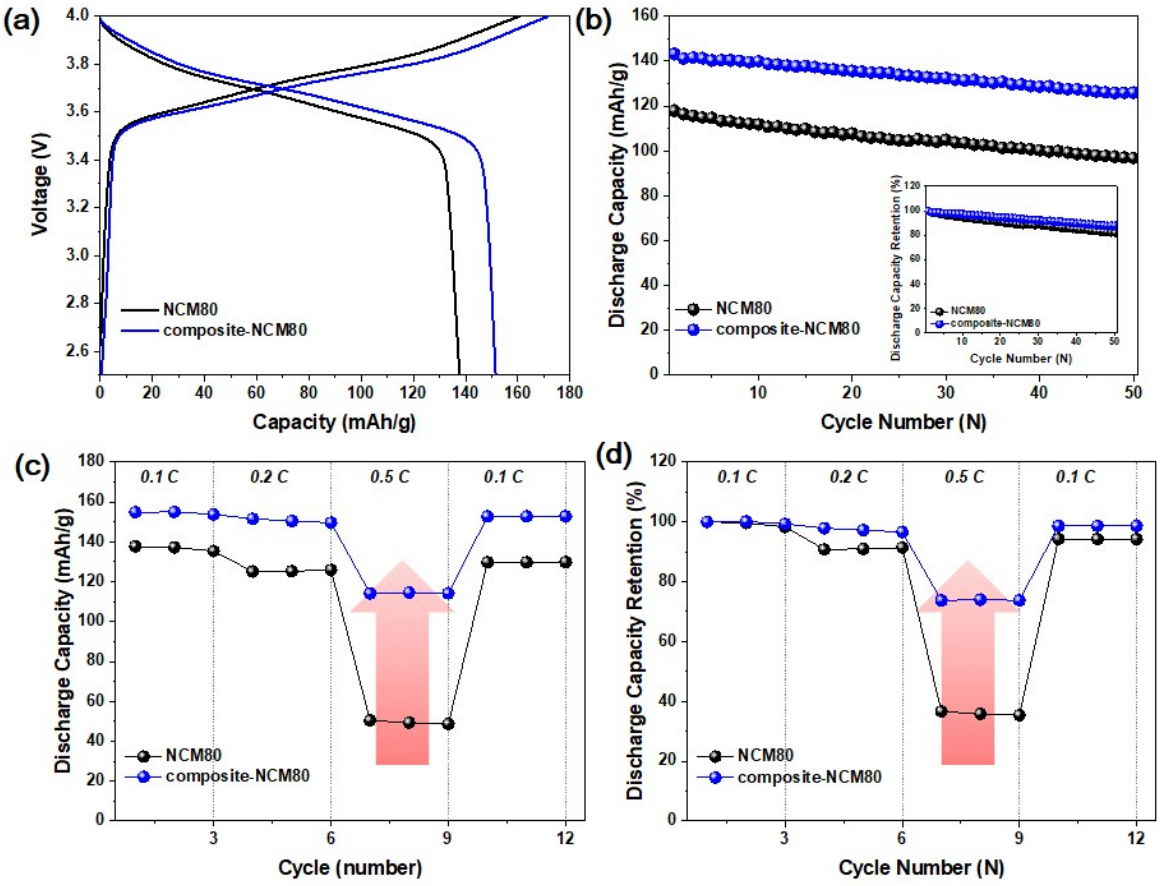

View Article Online
DOI: 10.1039/D0TA07347D

Fig 9

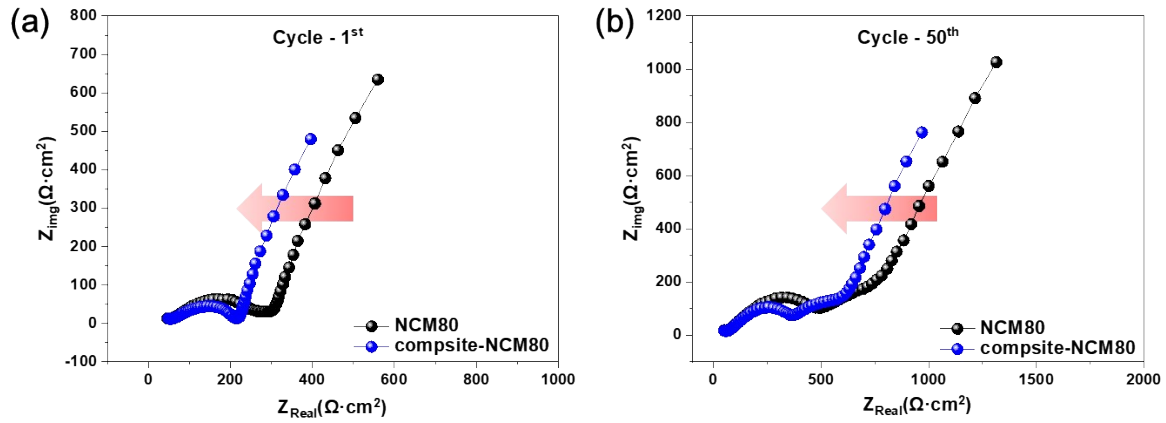

View Article Online
DOI: 10.1039/D0TA07347D

Fig 10

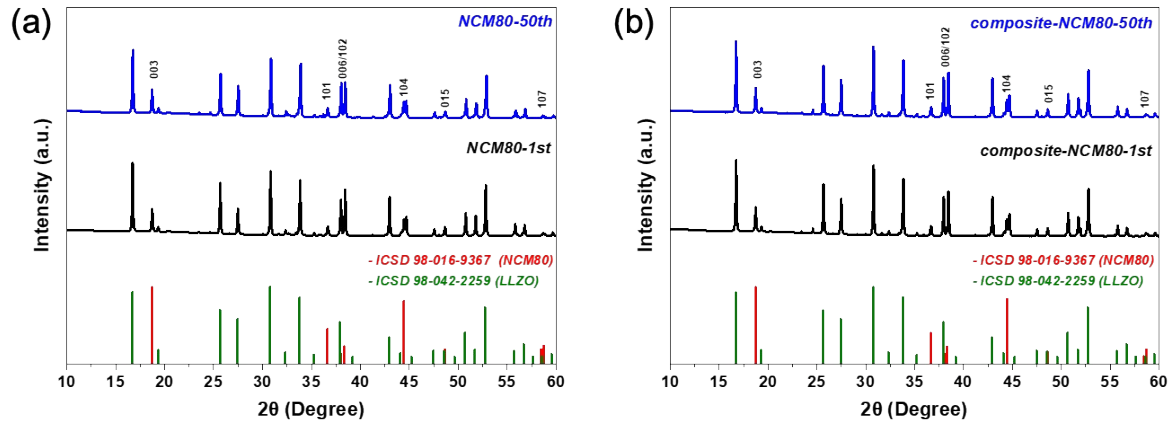

View Article Online
DOI: 10.1039/D0TA07347D

Table 1

Sample	a (Å)	c (Å)	c/a	$I_{(003)}/I_{(104)}$
NCM80	2.86942	14.19565	4.947219	1.5046
Composite-NCM80	2.87074	14.20124	4.946892	1.5896

View Article Online
DOI: 10.1039/D0TA07347D

Table 2

Sample	Li_2CO_3 (ppm)	LiOH (ppm)
NCM80	647	520
Composite-NMC80	219	280

View Article Online
DOI: 10.1039/D0TA07347D

Table 3

Sample	Li	Ni	Co	Mn	La	Zr	Al
LNCM80	1.04	0.791	0.108	0.101	-	-	-
Composite-NCM80	1.089	0.753	0.099	0.11	0.0015	0.0009	0.00072

View Article Online
DOI: 10.1039/D0TA07347D

Table 4

Sample	1st Cycle			50th Cycle		
	R_1 (Ω)	R_2 (Ω)	R_3 (Ω)	R_1 (Ω)	R_2 (Ω)	R_3 (Ω)
LNCM80	46.41	43.34	201.96	49.09	446.74	285.36
Composite-NCM80	49.16	44.49	130.55	49.64	286.54	246.9